Simulation of filtration processes in deformable media

Part 3.2: Interaction modelling and verification of a non-spherical dirt particle solver

Gernot Boiger[1], Marianne Mataln[1], Wilhelm Brandstätter[2]
[1] ICE Strömungsforschung GmbH, Hauptplatz 13, 8700 Leoben, Austria
[2] Montanuniversität Leoben, Franz-Josefstrasse 18, 8700 Leoben, Austria
www.ice-sf.at

ABSTRACT

A Lagrangian solver to realistically model large, non-spherical dirt particles and their behavior in the vicinity of deformable filtration fibres has been programmed. While this paper focuses on the realization of interaction effects and result verification, a related article, concerning basic solver concepts as well as drag force implementations, has been published, [3].

A digitally reconstructed, deformable filter fibre structure gives the framework for all particle interactions with their surroundings. Particle–fibre deposition effects, are being modelled in detail. Fibre forces, that act on a particle and confine it, can be applied on a user-defined basis. The *collision module* handles particle–particle interactions, detects exact particle-surface impact locations and calculates translational- as well as rotational collision effects.

In order to validate Computational Fluid Dynamics results, like filter fibre efficiency and particle penetration depth, a semi-analytical verification approach for simplified fibre geometries has been devised. In addition to that, extensive, experimental test runs are currently conducted.

1 INTRODUCTION

The Open Source Computational Fluid Dynamics (CFD) toolbox OpenFOAM® has served as a programming environment for the development of a novel, deterministic, micro scale, fluid-particle-fibre filtration solver [1], [2]. This C++ based simulator is supposed to become an important tool for the CFD design of filter media for automotive lubrication. It was created to consider all physically relevant effects that go along with, or lead to a micro scale, dirt particle deposition in a realistically reconstructed filtration fibre geometry.

Concerning this subject, three articles, have been previously published. While [1] focuses on fibre deformation and fluid–structure interaction (FSI) effects, [2] describes the development of a large, spherical particle model for filtration applications. The third article [3] is a direct prequel to this work. A significant extension of the spherical dirt particle model, formulated in [2] is presented there. It describes the basic concepts and the essential drag force implementation method behind our novel, deterministic, Lagrangian, non-spherical particle

model. This work however, primarily focuses on how particle interaction with its surroundings is handled. The second, essential topic deals with the creation of a simplified, semi-analytical approach to verify solver functionality and result quality.

The main aspects of the development effort behind this paper are:

- Implementation of a detailed particle–fibre interaction- and deposition model.
- Creation of a non-spherical particle collision model, including exact impact-point determination as well as the consideration of rotational collision effects.
- Programming of Python [11] based evaluation utilities, to extract essential data on result parameters (such as filter fibre efficiency and particle penetration depth) from OpenFoam® text file output.
- Device of a semi-analytical scheme to verify solver functionality and result quality, within the framework of simplified fibre geometries.

1.1 BASIC CONCEPTS OF THE NON-SPHERICAL FILTRATION SOLVER

The framework for CFD analysis of the filter region is given by digitally reconstructed fibre geometries that are transformed to structured grid meshes by Matlab® utilities. A fluid-structure-interaction utility can handle fibre deformation effects on the basis of a stiff, explicitly coupled, single solver approach, [1], [10].

Because of the geometry range of ~200µm, the highly viscous, Newtonian oil current with a kinematic viscosity of $\eta_f \sim 10^{-4} m^2/s$ and relatively slow flow velocities ($u_f < 0.4 m/s$), the local Reynolds numbers Re in the fibre vicinity are expected to be mostly below 0.5, but surely below 1.0. Furthermore Knudsen numbers Kn range well below 0.015. Thus continuum equations are valid and the consideration of diffusion effects on particle motion becomes unnecessary, [14]. Hence, a simple, incompressible, laminar and isothermal fluid solver can handle the fluid situation.

The accurate modelling of dirt particle motion and interaction, as well as fibre deposition is of main concern. It has been found that particle-shape effects play an important role in filtration applications. A direct comparison of spherical and non-spherical particle filtration behaviour leads to significant deviations in filter fibre efficiency. The reasons for that are varying drag-force-to-mass-ratios [3] as well as slip- and bulk effects (see chapter 1.2 and 1.3). This is why, in extension of the previously published, spherical particle model [2], a highly detailed, more sophisticated and more accurate, non-spherical particle model had to be created.

Regardless of their shape, all particles of equal mass feature the same *diameter of a mass equivalent sphere* D_{sph}, which is defined as:

$$D_{sph} = \sqrt[3]{\frac{6m_p}{\pi\rho_p}} \tag{1}$$

In [4] the shape parameter α_{ax} was introduced to characterize the deviation of the three particle half axis of length a, b and c around D_{sph} as:

$$\alpha_{ax} = \frac{\sqrt{\left(2a - D_{sph}\right)^2 + \left(2b - D_{sph}\right)^2 + \left(2c - D_{sph}\right)^2}}{3D_{sph}} \tag{2}$$

The higher α_{ax}, the further the particle is from sphericity. Direct comparison of the filtration behaviour of particles with equal D_{sph} and varying α_{ax} gives insight into the relevance of non-spherical particle modelling. So far, two main shape effects with influence on filter fibre efficiency E have been identified:

- The non-spherical particle slip effect.
- The non-spherical particle bulk effect.

1.2 THE NON-SPHERICAL PARTICLE SLIP EFFECT

Longish, non-spherical particles with small, angular relaxation times τ_ω show a tendency to easily align themselves along the streamlines of the surrounding fluid. If D_p, D_b, D_c denote the axe diameters of an ellipsoid, so that $D_c \leq D_b \leq D_P$, then the smallest possible, projected, frontal area of an ellipsoid is given by:

$$A_{p,\min} = \frac{D_b D_c}{4}\pi \tag{3}$$

Particle alignment increases the likelihood of slipping through a pore of diameter D_F in a direction, perpendicular to $A_{p,min}$. Consequentially the two smaller axe diameters define the minimal pore size diameter $D_{F,min}$, that an aligning non-spherical particle can theoretically slip through:

$$D_{F,\min} = \sqrt{D_b D_c} \tag{4}$$

This means:

$$D_{F,\min} < D_P \tag{5}$$

The diameter of mass equivalent, spherical particles D_{sph} can also be written as:

$$D_{sph} = \sqrt[3]{D_P \cdot D_{F,\min}^2} \tag{6}$$

Which leads to the relation:

$$D_{F,\min} < D_{sph} \tag{7}$$

Thus the hydrodynamic *slip effect* of non-spherical dirt particles increases particle penetration depth and decreases filter fibre efficiency as compared to the case of mass equivalent, spherical particles.

For filtration simulation this means that a representation of non-spheres by mass equivalent spheres with diameter D_{sph} might lead to a considerable *overestimation* of the filter fibre efficiency. A representation by spheres of diameter D_p, on the other hand, will not only lead to an overestimation of filtration efficiencies, but will also result in wrong particle masses and consequentially in wrong calculations of over all particle hydrodynamics. Figure 1 presents a basic sketch of the situation.

1.3 THE NON-SPHERICAL PARTICLE BULK EFFECT

Longish, non-spherical particles with larger, angular relaxation times τ_ω show a tendency to hardly align themselves along the streamlines of the surrounding fluid. As a consequence the largest half axe diameter D_P commonly defines the minimal pore size diameter $D_{F,min}$ that the particle can slip through:

$$D_{F,\min} = D_P \tag{8}$$

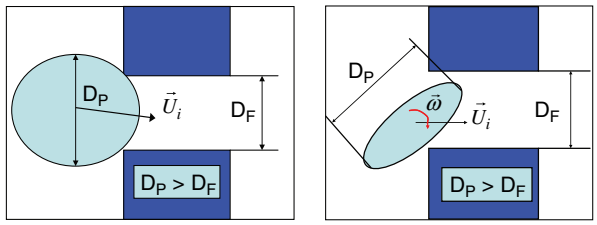

Figure 1 Non-spherical particle slip effect. Representation by spherical particles of diameter D_p (left) means overestimation of filtration efficiencies and particle mass as compared to the more realistic, non-spherical representation (right). The use of spheres with D_{sph} still leads to overestimation of filtration efficiencies because of Equ.7.

Since $D_p > D_{sph}$, a mass equivalent spherical particle might just slip through pores, that a bulky, non-spherical particle may not pass. Thus the hydrodynamic *bulk effect* of non-spherical dirt particles decreases particle penetration depth and increases filter fibre efficiency as compared to the case of mass equivalent, spherical particles.

In terms of filtration simulation this means that a representation of non-spheres by mass equivalent spheres with diameter D_{sph} might lead to a considerable *underestimation* of the filter fibre efficiency. Figure 2 presents a basic sketch of the situation.

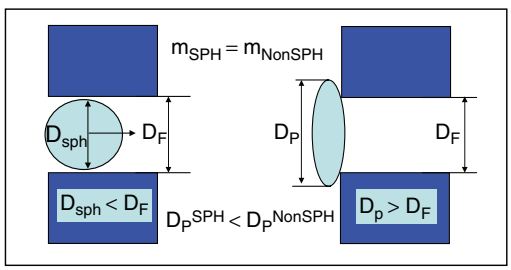

Figure 2 Non-spherical particle *bulk effect*. Representation by mass equivalent, spherical particles of diameter D_{sph} (left) means underestimation of filtration efficiencies as compared to the more realistic, non-spherical representation (right).

The bottom line at this point is that a non-spherical particle model, capable of including particle shape effects as well as rotational particle alignment, gives a much more realistic insight into detailed interaction behaviour in the particle–fibre vicinity, than any spherical representation ever can.

2 PARTICLE INTERACTION EFFECTS – EVENT FORCES

Particle-fluid interaction through drag- and lift forces is an essential aspect of Lagrangian modelling. Two drag modules, to be used for either the *free flow regime* or the *fibre vicinity domain*, have been developed. They are thoroughly discussed in [3].

Forces with influence on particle motion, that occur due to individual impact events, are hereby called *event or impact forces*. They represent particle-wall, particle–particle and particle-fibre interaction effects.

All N impact forces with relevance for particle motion occur within infinitesimal time scales that are smaller than numeric fluid time steps Δt_f or particle time steps Δt_p.

2.1 PARTICLE-WALL INTERACTION

Particles of mass m_p that hit a wall boundary patch and feature translational velocity u_p as well as angular velocity ω_p are reflected with user definable elasticity E_w. The reflection is performed by the use of a wall event force F_{wall}. Wall impact forces have already been introduced to handle spherical particle-wall interaction [2]. Now the concept has to be extended in order to consider rotational effects, particle orientation, the moment of inertia I_p and the exact (or at least approximated) point of impact at the particle surface. In Figure 3 the basic difference in spherical and non-spherical particle-wall impact is sketched out.

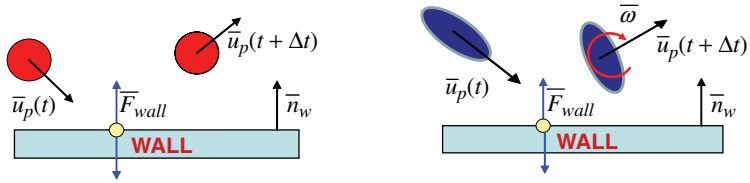

Figure 3 Sketch of spherical (left) and non-spherical (right) particle-wall impact. Non-spheres experience rotational as well as translational acceleration at impact.

To sense the impact location, the help points, with distance vector r_i to the particle centre are used and F_{wall} is modelled as:

$$\bar{F}_{wall} = -\frac{1+E_w}{\Delta t_p}\frac{\left(\bar{u}_p+\bar{\omega}_p\times\bar{r}_i\right)\cdot\bar{n}_w}{\frac{1}{m_p}+\frac{1}{I_p}\left[\left(\bar{r}_i\times\bar{n}_w\right)\times\bar{r}_i\right]\cdot\bar{n}_w}\cdot\bar{n}_w \tag{9}$$

Note that F_{wall} always acts perpendicular to the wall boundary patch, whereas fibre forces F_{fibre} (see chapter 2.2) also have components parallel to the boundary patch. Impact elasticity E_w has decisive influence on the translational and rotational impact behaviour of the particle. In Figure 4 the situation before and after impact is sketched out. The difference between completely elastic ($E_w = 1$) and completely plastic ($E_w = 0$) impact scenario is shown.

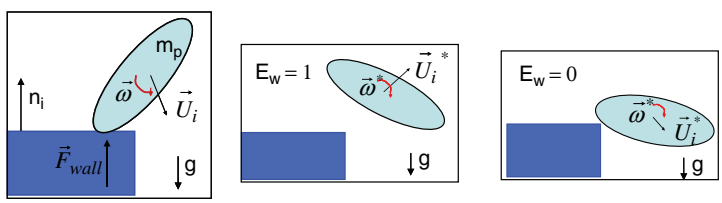

Figure 4 Qualitative sketch of the influence of non-spherical impact elasticity on particle-wall impact situation.

Screenshots of a qualitative benchmark case are shown in Figure 5. Here a simplified, fibre-like object in the particle flow path has been prescribed the *wall boundary condition* and thus serves as obstacle. An oval shaped ellipsoid hits the obstacle and is affected by the wall impact force. Consequentially its translation and rotation is altered.

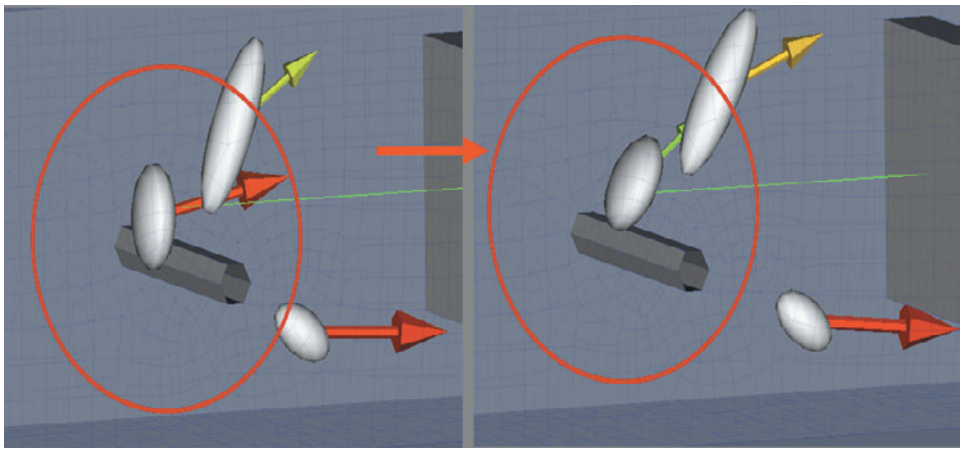

Figure 5 Screen shot of benchmark case. Ellipsoid particle just before (left) and after (right) hitting a wall boundary patch. Particle experiences rotational and translational acceleration.

2.2 PARTICLE-FIBRE INTERACTION AND PARTICLE DEPOSITION MODEL

The modelling of particle interaction with filter fibres and deposition mechanisms is essential. Due to the non-stochastic nature of the particle solver, no simplifying deposition model as in [5] or [6] is applied. Each particle is treated as dynamically interacting individual, according to its momentum, acting hydrodynamic- or event forces as well as fibre forces, which restrain its movement. Thus every increase of hydrodynamic- or event forces can lead to a particle blow-off.

Supposedly a fibre material that shows any particle adhesion at all, can restrain any infinitesimally small particle (D_{sph}<<) that hits the fibre.

It is plausible to assume that there is a maximum, possible amount of fibre force F_{fibre} on the particle and that it is directly proportional to the contact area, which is again proportional to D_{sph}^2. Fibre forces eliminate particle momentum, which is proportional to D_{sph}^3 and act against hydrodynamic drag which under *Stokes* flow conditions is roughly proportional to D_{sph}^2. As a consequence, particles will be harder to stop, as D_{sph} gets larger. Above a certain *ìsticking diameterî* D_{stick}, particles will deposit according to a probability density distribution function (PDDF) that can be derived from experiments. The task within solver design is to integrate any, user definable PDDF of the form seen in Equ.16 into the concept of deterministic particle-fibre interaction force deposition.

A particle-fibre interaction module has been created. It distinguishes between three modes of interaction: the impact-, the gliding- and the full stop- or deposition phase.

Impact phase

When a particle–fibre impact occurs, $F_{fibre,impact}$ acts just like F_{wall} for completely plastic ($E_w = 0$) impact and can be written as:

$$\overline{F}_{fibre,impact} = -\frac{\left(\overline{u}_p + \overline{\omega}_p \times \overline{r}_i\right)\cdot \overline{n}_w}{\Delta t_p \cdot \left(\frac{1}{m_p} + \frac{1}{I_p}\left[\left(\overline{r}_i \times \overline{n}_w\right)\times \overline{r}_i\right]\cdot \overline{n}_w\right)} \cdot \overline{n}_w \qquad (10)$$

$F_{fibre,impact}$ is designed to momentarily remove the particle help point velocity component perpendicular to the wall $u_{p,i}^{\perp}$. For the particle mass centre this means that the velocity

component perpendicular to the wall $u_{pi}^{\perp}$ is reduced and that a particle moment of impact $M_{fibre,impact}$ causes the particle to rotate around the impact point (see Figure 6).

Gliding phase

As long as the particle detects fibre contact and still retains $|u_{p,||}| > 0$, it glides along the fibre surface. The decelerating fibre counter force $F_{fiber,gliding}$ now acts in opposite direction of $u_{p,||}$ and is proportional to D_{sph}^2, the amount $|u_{p,||}|$ and a user definable material, fibre force constant D_{ff}, so that:

$$\overline{F}_{fibre,gliding} = -D_{ff} \cdot D_{sph}^2 \cdot \overline{u}_{p,||} \tag{11}$$

The pre- and post impact situation is sketched out in Fig.6.

In Figure. 6 Δt_p is the numerical particle sub-time step.

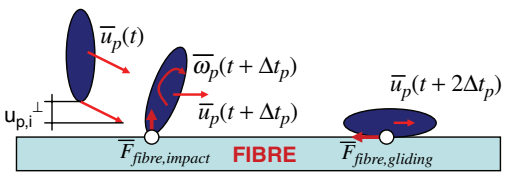

Figure 6 Sketch of a non-spherical particle-fibre impact/interaction situation. Ellipsoid just before (left) and after (middle, right) fibre impact. At impact particle is affected by $F_{fibre,impact}$, rotation around impact point, towards fibre sets in (middle). Particle then decelerates (glides) along surface, being restrained by $F_{fibre,gliding}$.

Full stop-/deposition phase

Particle acceleration into the opposite direction, due to $F_{fiber,gliding}$ would be unphysical. Therefore the reversal of velocity direction, or the deceleration below a user defined, very low, *stop velocity* u_{stop} make a valid criterion for a particle being deposited or not. The reversal condition states that the ratio of numerical particle velocity-change due to fibre force $|\Delta u_{p,||}|$ during Δt_p, and $|u_{p,||}|$ equals 1, which means:

$$\frac{\left|\Delta \overline{u}_{p,||}\right|}{\left|\overline{u}_{p,||}\right|} \overset{!}{=} \frac{6 D_{ff} \Delta t_p}{D_{sph} \pi \rho_p} \overset{!}{=} 1 \tag{12}$$

A *stop number* N_{stop} is introduced, that contains both, the reversal condition and a *stop velocity* condition so that:

$$N_{stop} = \frac{6 D_{ff} \Delta t_p}{D_{sph} \pi \rho_p} + \frac{u_{stop}}{\left|\overline{u}_{p,||}\right|} \tag{13}$$

Here the *stop velocity* condition $u_{stop}/|u_{p,||}|$ merely serves as break up condition for the convergence of particle velocity to *zero*. Therefore u_{stop} should be set $<<u_f$.

The final deposition condition is:

$$N_{stop} \overset{!}{\geq} 1 \tag{14}$$

Disregarding the *stop velocity* condition, this leads to the definition of the particle *stop diameter* D_{stop}:

$$D_{stop} = \frac{6 D_{ff} \Delta t_p}{\pi \rho_p} \tag{15}$$

A particle with $D_{sph} \leq D_{stop}$ will be stopped and deposited with deposition probability $\Phi_d(D_{sph}) = 1$, as soon as a fibre is touched. A particle with $D_{stop}<D_{sph}<D_{siev}$ yields higher momentum and larger hydrodynamic forces and therefore is deposited with a probability $0<\Phi_d<1$. D_{siev} marks a particle diameter below which sieving effects are still irrelevant for particle deposition. The PDDF $\Phi_d(D_{sph})$, given by Equ.16 is supposed to be user definable and is based upon a simple, Gaussian-Normal distribution [13], defined by the two parameters: average D_{stop} and standard deviation σ_d.

$$\underset{D_{stop}<D_{sph}<D_{siev}}{\wedge} \Phi_d\left(D_{sph}\right) = \frac{1}{\sigma_d \sqrt{2\pi}} e^{-\frac{\left(D_{sph}-D_{stop}\right)^2}{2\sigma_d^2}} \tag{16}$$

The standard deviation is given via a third, user definable deposition constant σ_{slope}. The solver basically features three optional deposition modules:

1.) No adhesion-based deposition for $D_{sph} > D_{stop}$:

$$\sigma_d \to 0 \tag{17}$$

2.) σ_d depends directly on the user defined σ_{slope}:

$$\sigma_d = \sqrt{\frac{\sigma_{slope}}{2}} \tag{18}$$

3.) σ_d depends not only on the user defined σ_{slope} but also on fluid/particle properties and D_{ff}:

$$\sigma_d = \sqrt{\frac{D_{ff} \cdot 10^{\sigma_{slope}}}{2\rho_p \eta_f}} \tag{19}$$

In order to decide whether the individual particle with $D_{sph} > D_{stop}$, featuring a deterministic deposition probability $\Phi_d(D_{sph})$, is actually deposited at fibre contact, the stop parameter P_{stop} is defined by comparing Φ_d to a randomized, rectangularily distributed variable Φ_{01}.

$$P_{stop} = \Phi_d\left(D_{sph}\right) - \Phi_{01} \cdot \frac{1}{\sigma_d \sqrt{2\pi}} \tag{20}$$

The deposition condition is then:

$$P_{stop} \overset{!}{\geq} 0 \tag{21}$$

The bottom line at this point is:

1) Any particle that touches a fibre experiences $F_{fibre,impact}$ and looses its velocity component perpendicular to the fibre surface.
2) Any particle that touches a fibre experiences $F_{fibre,gliding}$ which reduces its velocity parallel to the fibre surface.
3) There are three ways for a particle to get deposited at fibre contact.

a) The diameter of a volume equivalent sphere is below the stop diameter:

$$D_{sph} \le D_{stop}\left(D_{ff}, \Delta t_p, \rho_p\right) \;\rightarrow\; N_{stop} \ge 1 \tag{22}$$

b) Due to the effect of $F_{fibre,gliding}$ the particle velocity falls below the stop velocity:

$$u_{p,\|} \le u_{stop} \rightarrow \; N_{stop} \ge 1 \tag{23}$$

c) The stop number is smaller than 1 but the particle fulfils the stop parameter condition:

$$N_{stop} < 1 \;\wedge\; P_{stop} \ge 1 \tag{24}$$

Any particle which fulfils either condition 3a, 3b or 3c will be deposited and is subject to a fibre constraining force $F_{fibre,constrain}$ that brings the remaining movement of the particle-fibre contact point to a halt:

$$\overline{F}_{fibre,constrain} = -\frac{\left(\overline{u}_p + \overline{\omega}_p \times \overline{r}_i\right)\cdot \overline{e}_{up,i,\|}}{\Delta t_p \cdot \left(\frac{1}{m_p} + \frac{1}{I_p}\left[\left(\overline{r}_i \times \overline{e}_{up,i,\|}\right)\times \overline{r}_i\right]\cdot \overline{e}_{up,i,\|}\right)} \cdot \overline{e}_{up,i,\|} \tag{25}$$

Here $e_{up,i,\|}$ is the base vector for the velocity of contact point i, $u_{p,i,\|}$ and r_i is the distance vector of contact point i to the particle mass centre.

The occurrence of additional particle forces F_i can still speed up the particle, so that condition 3b is void and $F_{fibre,constrain}=0$ or so that $F_{fibre,constrain}$ still is >0, but is outmatched by the N-1 other acting forces. A blow off would be the consequence. It is up to the user to decide whether the consideration of *blow off* effects is relevant, or whether adhesional deposition probability should work strictly governed by Φ_d. The latter choice requires a more rigid fibre constraining force $F_{fibre,constrain,rigid}$:

$$\overline{F}_{fibre,constrain,rigid} = -\frac{\left(\overline{u}_p + \overline{\omega}_p \times \overline{r}_i\right)\cdot \overline{e}_{up,i,\|}}{\Delta t_p \cdot \left(\frac{1}{m_p} + \frac{1}{I_p}\left[\left(\overline{r}_i \times \overline{e}_{up,i,\|}\right)\times \overline{r}_i\right]\cdot \overline{e}_{up,i,\|}\right)} \cdot \overline{e}_{up,i,\|} - \sum_{i=1}^{N-1} \overline{F}_i \tag{26}$$

Numerical evaluations of adhesion-based filter fibre efficiency curves, on simplified, single fibre geometries have been conducted as seen in Figure 7. The test cases already include all the important dynamic interactions between particles, fluid, walls and fibres. Results clearly show, that the task of embedding externally imposed PDDFs Φ_d, to include experimentally studied particle-fibre interaction properties, into an otherwise discrete, deterministic system of force interactions, has been accomplished. Up to 100 mono disperse, non-spherical particles have been injected, just upstream of a simplified fibre geometry, seen in Figure 7. Injection position and Stokes number St of each particle are chosen such that the hitting of a fibre is assured. Otherwise injection is arbitrary. A deposition probability curve has been pre-defined as seen in Figure 8. Repeating the run with particles featuring varying, relevant diameters D_{sph}, deposition efficiencies E for each particle class have been evaluated. As shown in Figure 8, the results match quite well.

2.3 PARTICLE–PARTICLE INTERACTION

Within the fibre vicinity, high particle cloud densities occur. As more and more particles get entangled in the fibre, their volume fraction increases and particle-particle interactions

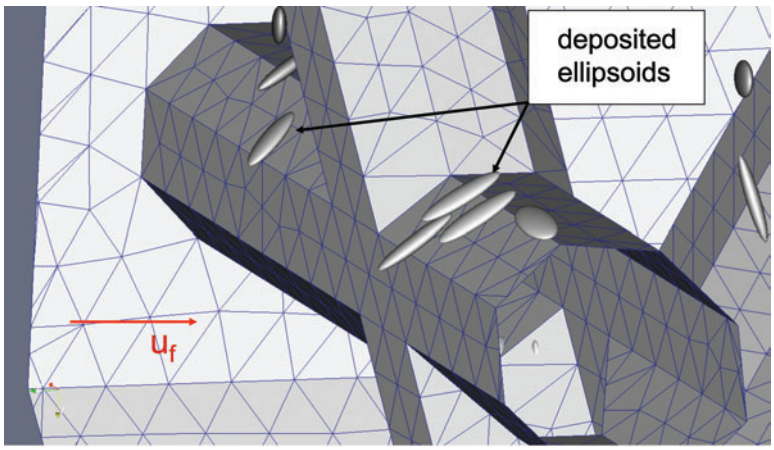

Figure 7 Benchmark case to test particle-fibre interaction module. Simple fibre geometry with ellipsoids being deposited due to particle-fibre adhesion.

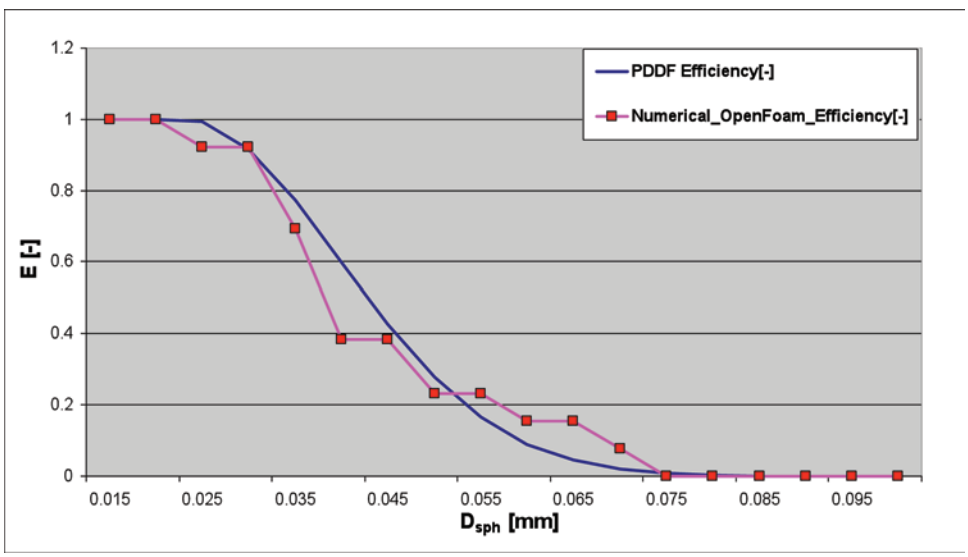

Figure 8 Adhesion-based, filter fibre efficiency for the simplified fibre structure case seen in Figure 7. Pre-defined PDDF for adhesion based deposition (blue) compared to numerical results (purple).

become relevant. While hydrodynamic interaction is handled by the fibre *vicinity drag module* (local plugging, [2], [3]), physical interactions (i.e. collisions) have to be considered as well.

As soon as a particle enters the fibre vicinity, its data (particle mass centre X_p, orientation of particle x- and y axis, e_x, e_y, particle mass m_p, and particle half axe diameters a, b, c) is stored in a dynamic *collision list*. It is now a potential collision partner. The help point method, [3] is used to actually realise accurate, ellipsoid collision calculation.

If any help point HP^A of particle A detects an impact with particle B, the following procedure is initiated:

1.) Calculation of impact point IP^B on particle B (not necessarily a particle help point HP^B). IP^B is determined as the intersection point of ellipsoid B and a straight line through HP^A and $X_p{}^B$. The problem is transformed into the co-rotational coordinate system of particle B where $X_p{}^B = 0$, so that IP^B is:

$$IP^B{}' = HP^A{}' \frac{a^B \cdot b^B \cdot c^B}{\sqrt{x^{HP,A}{}' a^B c^B + y^{HP,A}{}' a^B c^B + z^{HP,A}{}' a^B b^B}} \tag{27}$$

Note that the superscript ë stands for coordinates within the co-rotational particle coordinate system. The concept of the co-rotational particle coordinate system is thoroughly described in [3].

2.) Determination of collision vector n_{coll}. Due to the help point discretization of the ellipsoid particle surface, an exact calculation of surface normal vectors at impact points of particle A and B, would not yield two vectors of the same direction. An exact determination of ellipsoid surface normal n_B of particle B at IP^B is necessary to give the impact an appropriate direction. The calculation is performed within the co-rotational coordinate system of particle B and looks like:

$$\bar{n}_{coll}{}' = \bar{n}_B{}' = \frac{z^{IP,B}{}'}{\left|z^{IP,B}{}'\right|} \cdot \frac{1}{\sqrt{f_{Bxz}{}^2 + f_{Byz}{}^2 + 1}} \left(f_{Bxz}, f_{Byz}, 1\right) \tag{28}$$

Here f_{Bxz} and f_{Byz} are:

$$f_{Bxz} = -\frac{z^{IP,B}{}'}{\left|z^{IP,B}{}'\right|} \cdot \frac{c^2 \cdot x^{IP,B}{}'}{a^2} \sqrt{c^2 \left| 1 - \left(\frac{x^{IP,B}{}'}{a^2}\right)^2 - \left(\frac{y^{IP,B}{}'}{b^2}\right)^2 \right|} \tag{29}$$

$$f_{Byz} = -\frac{z^{IP,B'}}{\left|z^{IP,B'}\right|} \cdot \frac{c^2 \cdot y^{IP,B'}}{b^2} \sqrt{c^2 \left| 1 - \left(\frac{x^{IP,B'}}{a^2}\right)^2 - \left(\frac{y^{IP,B'}}{b^2}\right)^2 \right|} \tag{30}$$

3.) Modelling of the collision force $F_{collision}$. The collision force is designed to either reverse (100% elastic impact) or eliminate (100% plastic impact) the relative velocity $u_{p,rel}$, between HP^A and IP^B according to user-defined impact elasticity E_{coll}. The direction of F_{coll} is given by n_{coll}. It obviously has to be reversed for collision force calculation for either one of the two collision partners. F_{coll} for particle A then reads:

$$\bar{F}_{Coll}^A = \frac{-\left(1 + E_{coll}\right) \cdot \left[\left(\bar{u}_P^A - \bar{u}_P^B\right) + \left(\bar{\omega}_P^A \times \bar{r}^{HP,A} - \bar{\omega}_P^B \times \bar{r}^{IP,B}\right)\right] \cdot \bar{n}_{coll}}{\Delta t_p \left[\frac{\bar{n}_{coll}}{m_P^A} + \frac{\bar{n}_{coll}}{m_P^B} + \frac{1}{I_P^A}\left(\bar{r}^{HP,A} \times \bar{n}_{coll}\right) \times \bar{r}^{HP,A} + \frac{1}{I_P^B}\left(\bar{r}^{IP,B} \times \bar{n}_{coll}\right) \times \bar{r}^{IP,A}\right] \cdot \bar{n}_{coll}} \cdot \bar{n}_{coll} \tag{31}$$

Here $r^{HP,A}$ stands for the distance vector of HP^A to $X_{P,A}$ and $r^{IP,B}$ stands for the distance vector of IP^B to $X_{P,B}$. A similar collision force implementation is used by Shah & Megahed, [9]. A sketch of the non-spherical impact situation is shown in Figure 9.

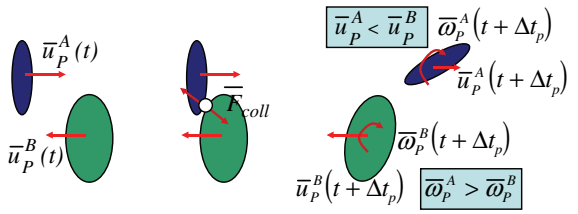

Figure 9 Sketch of impact situation with non-spherical particles A and B, before (left), during (middle) and after (right) collision. Post impact situation: The translational velocity of the smaller particle A is more strongly impaired and is smaller than that of particle B. The angular velocity of particle A is higher than that of particle B.

3 COMBINED NON-SPHERICAL FILTRATION SOLVER

Along with the results, published in [1]-[4], the solver module can be combined to a unified filtration simulator.

Figure 10 shows an exemplary screenshot of a benchmark case, which includes a dense cloud of non-spherical dirt particles, getting entangled in a realistically reconstructed, deforming filter fibre geometry. The screenshot gives a qualitative impression of what the solver can do.

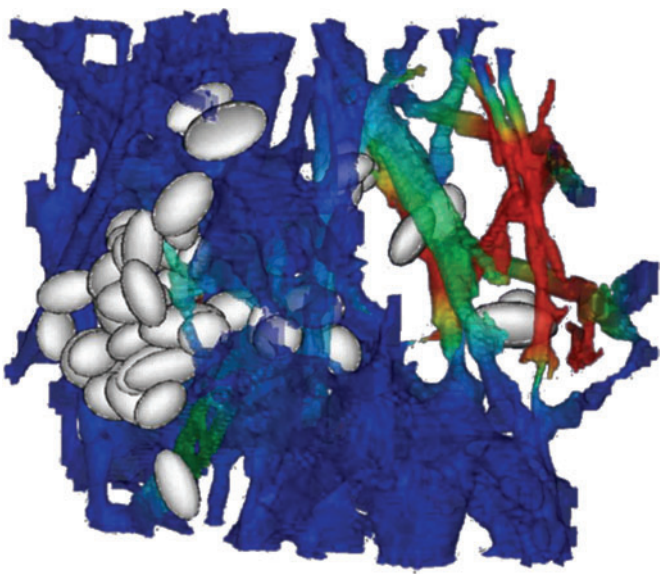

Figure 10 Screen shot of benchmark case. Dense cloud of non-spherical particles in realistic, deforming filter fibre geometry. Fibre vicinity drag module [3] is active, four-way coupling is engaged, deposition mechanisms initiated and FSI utility [1] is switched on.

4 SOLVER VERIFICATION AND RESULTS

Solver verification can only occur by comparison of statistically averaged results. Crucial process parameters such as pressure drop, filter fibre efficiency and penetration depth are the key to comparing calculations and experiment.

4.1 NUMERICAL AND SEMI-ANALYTICAL FILTER FIBRE EFFICIENCY CURVE

A first, important step in validating qualitative aspects of solver functionality can be taken by comparing CFD calculations and semi-analytical results for artificially created, simplified fibre geometries. The process parameter to be chosen for benchmarking is filter fibre efficiency E. It is defined by:

$$E_i = n_{s,i}/n_i \tag{32}$$

Here E_i is the fractional filter fibre efficiency of size class i; n_i is the total number of dirt particles per size class i and $n_{s,i}$ is the number of dirt particles retained by the filter.

4.1.1 Simplified geometry

In order to be able to establish a well defined, semi-analytically derived filter fibre efficiency curve over the entire, relevant regime of particle sizes (2µm-200µm), a simplified fibre geometry has to be created. The main reasons for that are:

- Reduction of complexity to allow focus on main qualitative aspects of the solution.
- Lower computational cost for various test runs.
- Simpler determination of basic geometrical parameters than with realistic geometries. Geometrical parameters with relevance for the calculation are:
  - Frontal, free flow area due to pores, A_{pores}
  - Number of frontal, free flow channels, in other words: number of projected pores, n_{pores}
  - Pore size distribution: medium pore diameter (MPD) D_{pores} of projected, free flow area per pore; standard deviation around MPD, σ_{pores}
  - Medium fibre diameter D_{fibre}

Figure 11 shows an exemplary, simplified, 30.000 cell, fibre geometry, where all relevant geometrical parameters are easily determinable.

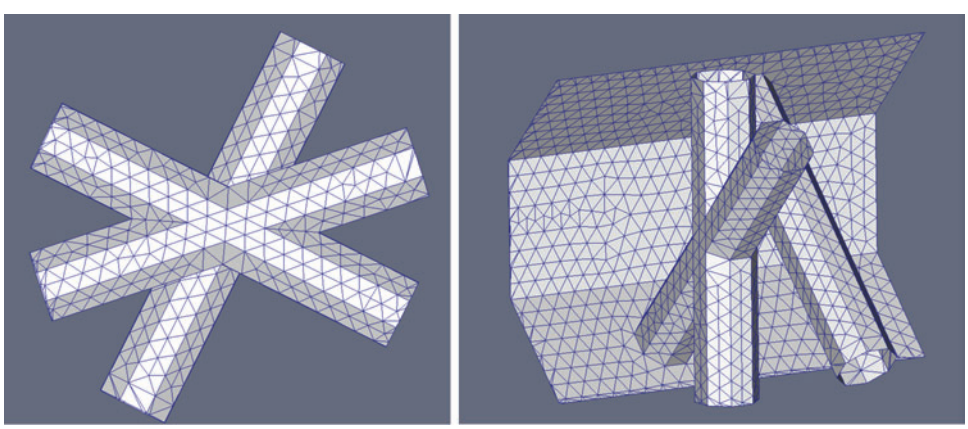

Figure 11 Exemplary image of simplified fibre geometry. Easy determination of geometrical parameters: A_{pores}, n_{pores}, D_{pores}, σ_{pores}, D_{fibre}.

4.1.2 Semi-analytical approach

The set up of a suitable, semi-analytical model for filter fibre efficiency calculation requires the integration of all relevant filtration aspects. The most relevant effects to be considered over a dirt particle size-range from 2µm to 200µm and particle Reynolds numbers Re_p well below 1 are:

- Inertial impact
- Particle–fibre adhesion
- Blow off due to particle momentum or interactions
- Sieving

The total particle deposition probability P_{Dep} of any particle (which is equivalent to E) can be calculated as a function of various *"single effect"* deposition contributions (see Equ.33). Hereby the *inertial impact* contribution is described by the hitting channel probability P_{HCh} and by the *inertial impact* probability P_{Stokes} which can be quantified via the Stokes Number St (see Equ.35). The *particle–fibre adhesion* as well as *blow off* effects can be considered via the particle sticking probability P_{Stick}. Sieving contributions to overall filter fibre efficiency are finally quantified over the pore size dependent, *flow path blocking probability* P_{Block}.

$$P_{Dep} = P_{HCh} P_{Stokes} P_{Stick} + \left(1 - P_{HCh} P_{Stokes} P_{Stick}\right) P_{Block} \tag{33}$$

Inertial impact effects

In order for any particle to impact on a fibre surface, two conditions will have to be satisfied:

1.) Particle must be on collision course.
2.) Particle inertia must be high enough to "break out" of fluid stream lines around fibre.

In the context of this work a particle is defined to be on collision course with a fibre as long as at least the fraction n of D_{sph} overlaps with a part of the projected, crossectional, fibre-covered area A_{Fibre} of the entire flow channel A_{FCh}. With knowledge of the projected, crossectional, free flow area due to pores A_{Pores} and the number of pores n_{Pores}, the hitting channel probability can be calculated as:

$$P_{HCh} = \left(\frac{A_{fibre} + 2 \cdot D_{sph} \cdot (1-n) \cdot \sqrt{A_{pores} \cdot n_{pores} \cdot \pi}}{A_{FCh}} \right) \tag{34}$$

Even if a particle is on collision course, impact is still not assured due to fluid deviation around the fibre. Larger particle inertia increases the likelihood of impacting anyway. The inertial impact probability P_{Stokes} can be characterized via the Stokes number [12], that gives a dimension less relation between inertial and viscous forces on the particle:

$$St = \frac{\rho_p D_{sph}^2 \left| u_{rel} \right|}{18 \eta_f \rho_f D_k} \tag{35}$$

Here D_k stands for the diameter of the collector, which in our case is the average fibre diameter D_{fibre}, ρ_p and ρ_f are the particle- and fluid density respectively and η_f is the kinematic fluid viscosity.

The minimal, critical, particle-fibre Stokes number St_{min} is defined as the level below which any particle, even though on collision course, is deviated around the fibre (see Figure 12a). The

maximum, critical Stokes number St_{max}, on the other hand, is hereby defined as the level above which any particle, whose course overlaps with at least the fraction n of D_{sph} with a fibre-covered area, impacts on the fibre structure (see Figure 12b).

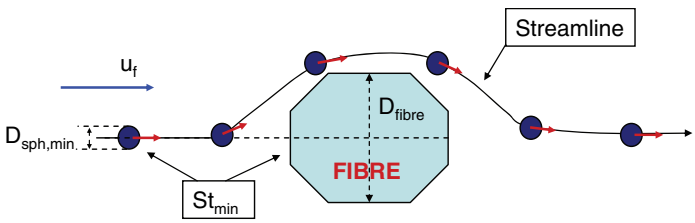

Figure 12a Definition of St_{min}. The largest particle on direct collision course that just passes by the fibre without hitting, defines St_{min}.

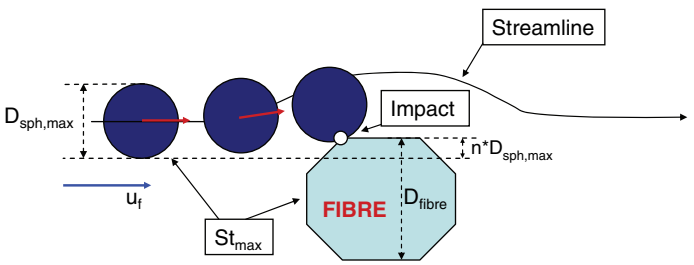

Figure 12b Definition of St_{max}. The smallest particle that just collides with the fibre, even though its collision course is just such that the n^{th} fraction of D_{sph} overlaps with a fibre, defines St_{max}.

Using those definitions, the inertial impact probability is in this work calculated as:

$$P_{Stokes} = \frac{St(D_{sph}) - St_{\min}}{St_{\max} - St_{\min}} \tag{36}$$

In order to obtain values for St_{min} and St_{max} a simple, numerical simulation where particles are set on a collision course with fibres of diameter D_{fibre} is used (equivalent to sketches in Figure 12a and 12b.) The parameter n is set to 1.0%. The overall hitting probability P_{hit} can now be semi-analytically determined and is:

$$P_{Hit} = P_{HCh} P_{Stokes} \tag{37}$$

For "small" particles with $D_{sph} < D_{stop}$, the hitting probability is equivalent to the deposition probability. For "larger" particles with $D_{sph} > D_{stop}$, other effects have to be taken into account as well.

Particle–fibre adhesion and blow off due to particle momentum or interactions

The user-definable, adhesional deposition probability for ìmedium sizedì particles with $D_{stop} < D_{sph} < D_{siev}$ is deeply incorporated into the force interaction scheme of the CFD solver (see chapter 2.2). For the sake of semi-analytical verification of solver

functionality, the underlying PDDF for particle-adhesional sticking probability P_{stick} is chosen. The same parameters (D_{stop}, σ_d) that are used in the CFD run are inserted, thus P_{stick} is calculated as:

$$P_{stick} = \frac{1}{\sigma_d \sqrt{2\pi}} e^{-\frac{\left(D_{sph}-D_{stop}\right)^2}{2\sigma_d^{\,2}}} \tag{38}$$

Sieving due to pore sizes

For "large" particles with $D_{sph} > D_{siev}$ the sieving effect is the most relevant reason for deposition. It is simply based upon the relation of particle diameter to pore size distribution $\sigma_{pores.}$ Underlying a Gauss-Normal distribution [13] of pore sizes, and using the geometrical parameters medium pore size D_{pores} and standard deviation σ_{pores}, the distribution function Φ_{pores} is given by:

$$\phi_{pores}\left(D_{sph}\right) = \frac{1}{\sigma \sqrt{2\pi}} e^{-\left(\frac{\left(D_{sph}-D_{pores}\right)^2}{2\sigma_{pores}^{\,2}}\right)} \tag{39}$$

The cumulative pore size distribution function is equivalent to the flow path blocking probability P_{Block} that can be calculated by use of the error-function erf:

$$P_{Block} = \int_{t=0}^{t=D_{sph}} \phi_{pores}\left(t\right) dt = \frac{1}{2}\left[1 + erf\left(\frac{D_{sph}-\mu_{pores}}{\sqrt{2}\sigma_{pores}}\right)\right] \tag{40}$$

Comparing CFD and analytical results

By using Equ.33 through Equ.40, the whole semi-analytical approach to describe the particle deposition probability within a simplified fibre geometry can be summarized as:

$$P_{Dep} = \frac{\left(St-St_{\min}\right)\left(A_{fibre}+2\cdot D_{sph}\cdot(1-n)\cdot\sqrt{A_{pores}\cdot n_{pores}\cdot\pi}\right)}{2\sqrt{2\pi}\sigma_d A_{FCh}\left(St_{\max}-St_{\min}\right)} e^{-\frac{\left(D_{sph}-D_{stop}\right)^2}{2\sigma_d^{\,2}}}\left[1-erf\left(\frac{D_{sph}-\mu_{pores}}{\sqrt{2}\sigma_{pores}}\right)\right] + \frac{1}{2}+\frac{1}{2}erf\left(\frac{D_{sph}-\mu_{pores}}{\sqrt{2}\sigma_{pores}}\right) \tag{41}$$

By inserting corresponding material-, and geometrical parameters into Equ.41, and into the input dictionaries of the CFD model, two comparable filter fibre efficiency curves are obtained. The results of the comparison are shown in Figure13. Semi-analytical results and CFD results match qualitatively and quantitatively. A verification of solver functionality is hereby considered to be achieved.

4.2 PRESSURE DROP

An experimental facility has been devised to test filter fibre samples in terms of essential process parameters. Pressure drop over filter life time and against flow rate variations can thus be monitored. The test results can then be directly compared to CFD runs, conducted on digitally reconstructed geometries of the same filter fibre material. So far an accordance of

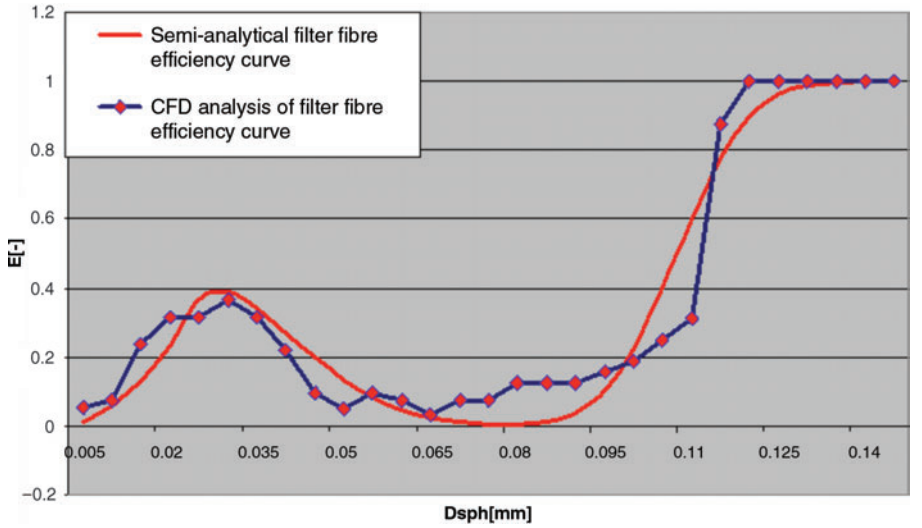

Figure 13 Comparison of filter fibre efficiency results for semi-analytical calculation (red) according to Equ. 41 and for CFD results (blue) using the non-spherical particle solver. The underlying, simplified geometry is depicted in Figure 11. Conditions: $\rho_f = 800 kg/m^3$, $\mu_f = 0.002 Pas$, $\rho_p = 1500 kg/m^3$, $u_f = 0.02 m/s$, $5 \mu m \leq D_{sph} \leq 150 \mu m$

+/–10% between lab tests and CFD runs has been achieved. More detailed results on pressure drop analysis will be published in the future.

4.3 APPLICATION AND (NON-) SPHERICAL RESULTS

In practice the CFD tool will rather be applied on realistically reconstructed, digitalized fibre geometries (as seen in Figure 14) than on simplified models. The means of result evaluation are manifold. Important insight into qualitative and quantitative aspects of process parameter behaviour, over filter life time can be gained. Two of the most interesting results are filter fibre efficiency- and particle penetration depth curves.

A typical example of solver application would be to take several, microscopic, digitally reconstructed portions out of a filter fibre sample and to conduct deposition- and

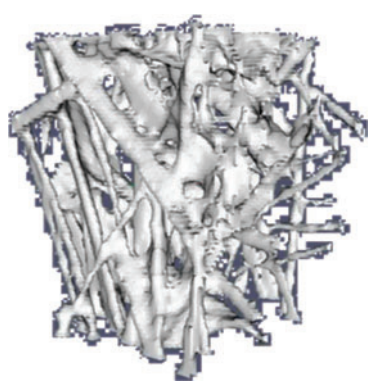

Figure 14 Example of an optically smoothed, digitalized fibre structure.

penetration analysis for the entire range of relevant particle sizes. The results would then be averaged in order to obtain an idea of the basic particle deposition characteristic of the fibre.

All relevant solver output data (such as pressure-/velocity field information, particle positions and orientation) is given in text files. Using Python [11] scripting, several evaluation modules have been created. Those modules use the text-based output data to extract result parameters (such as filter fibre efficiency and particle penetration depth).

To give an impression of what the solver can do as of now, three examples shall be considered.

4.3.1 Comparison of material with/without adhesional effects

The first example is supposed to point out the potential of the solver in terms of material design. A digitally reconstructed fibre geometry (see Figure 14) has been tested in interaction with clouds of arbitrarily shaped (non-spherical) particles with a half-axe standard deviation of $\alpha_{ax}=\sqrt{5/9}$. Filter fibre efficiency curves have been evaluated for two cases of fibre quality. Case a) features fibres that do not show any particle-fibre interaction, while case b) has the very same fibre topology, but includes particle-fibre adhesion. The results, seen in Figure 15, show a dramatic increase in filter efficiency (at equivalent pressure drop) if adhesional effects (and not just pore size distributions) are considered in material selection.

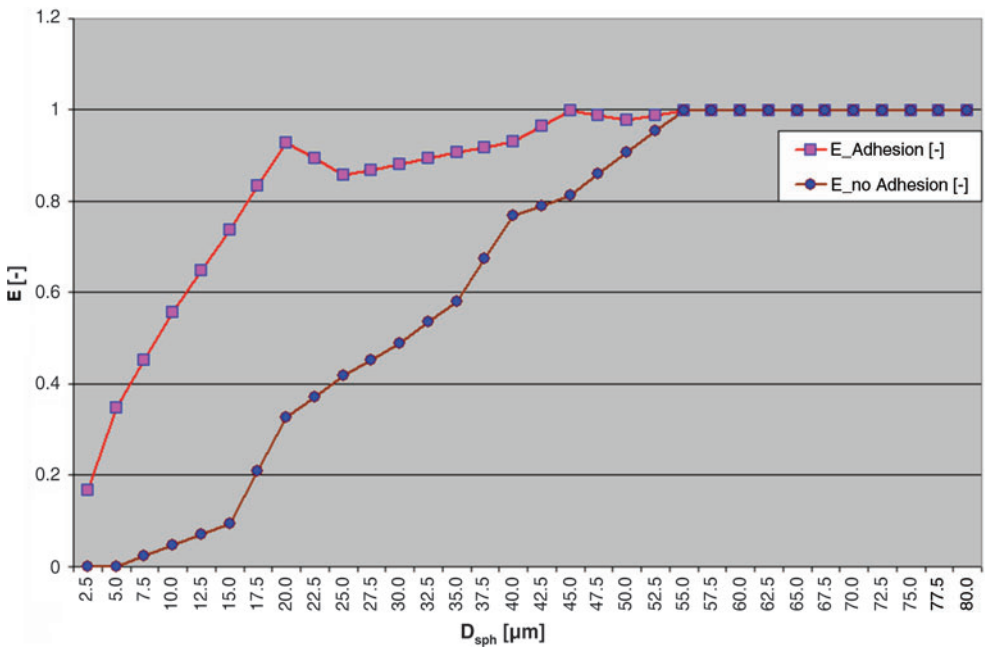

Figure 15 Comparison of filter fibre efficiency curves for one and the same fibre geometry. Case a) (red) is calculated with adhesional effects and case b) (brown) is calculated without. Test case parameters: geometry dimensions: 200µm*200µm*200µm; fluid: u_f=0.4m/s, ρ_f = 800kg/m^3, η_f=4*10^{-4} m^2/s; particles: ρ_p=3000kg/m^3, $\alpha_{ax}=\sqrt{5/9}$.

4.3.2 Comparison of (non-)spherical particle filter fibre efficiency

The second example shows the importance of considering non-spherical particle shape effects. Filter fibre efficiency curves, using spherical and non-spherical particles on one and the same, non-adhesional filter fibre medium (see Figure 14), have been evaluated. The ellipsoids feature a half-axe standard deviation of $\alpha_{ax} = \sqrt{5/9}$ and are always compared to their mass equivalent, spherical counterparts. The results, seen in Figure 16, point out the importance of considering particle shape effects. Relevant deviations in fibre efficiency are apparent.

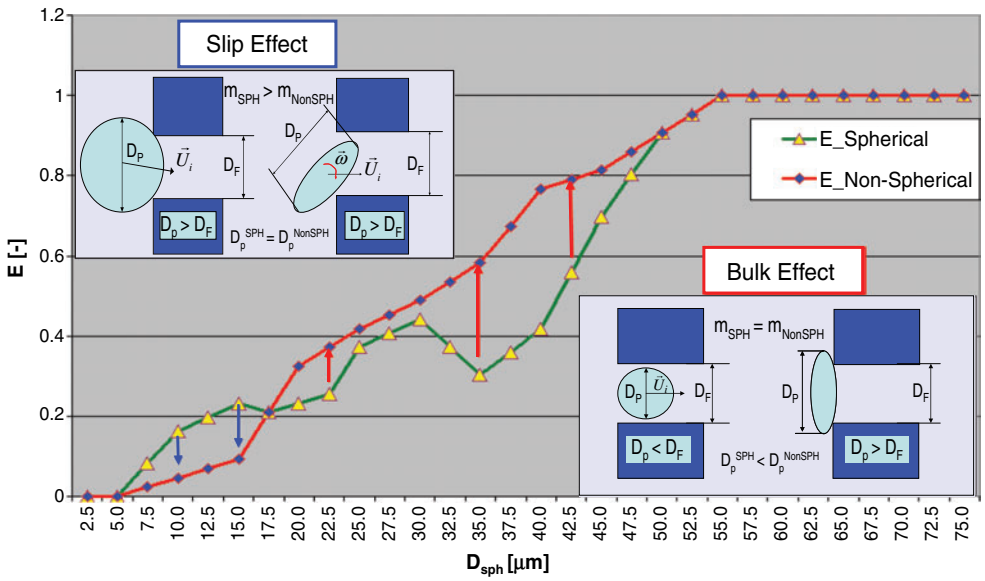

Figure 16 Comparison of filter fibre efficiency curves for one and the same fibre geometry without adhesional effects (equivalent to chapter 4.3.1, case b)). Case a) (green) is calculated with spherical particles and case b) (red) is calculated with non-spherical particles of mass equivalent spheres. Test case parameters match those, given for Figure 15.

Fibre efficiency results, shown in Figure 16, reveal that smaller ellipsoids ($D_{sph} < 17.5\mu m$) are deposited less easily than mass-equivalent spheres, whereas larger ($D_{sph} > 17.5\mu m$), non-spherical particles rather get stuck. This behaviour is both plausible and to be expected. Ellipsoids with smaller, angular relaxation times experience the *slip effect*. They align easily along current stream lines, which enables them to slip through pores, that mass-equivalent spheres get stuck in (see Figure 1 and chapter 1.2). Larger ellipsoids with larger, angular relaxation times do not align as readily and experience the *bulk effect*. They get stuck in pores that their spherical counterparts just fit through (see Figure 2 and chapter 1.3). Between 30µm and 37µm spherical filter fibre efficiency decreases. This phenomenon can be attributed to increasing particle-particle interactions due to higher particle-particle hitting probability. Momentum transfer leads to blow off effects.

4.3.3 Comparison of (non-)spherical particle penetration depth

The third example gives an evaluation of particle penetration depth for the spherical and non-spherical case shown in chapter 4.3.2 (both without adhesional effects) and for the non-spherical case, featuring adhesional effects, that is shown in chapter 4.3.1.

Hereby the particle penetration depth is represented via the relative penetration measure P that attributes the value 1 to particles slipping through the fibre mesh, and 0 to particles caught right at entry into the fibre vicinity.

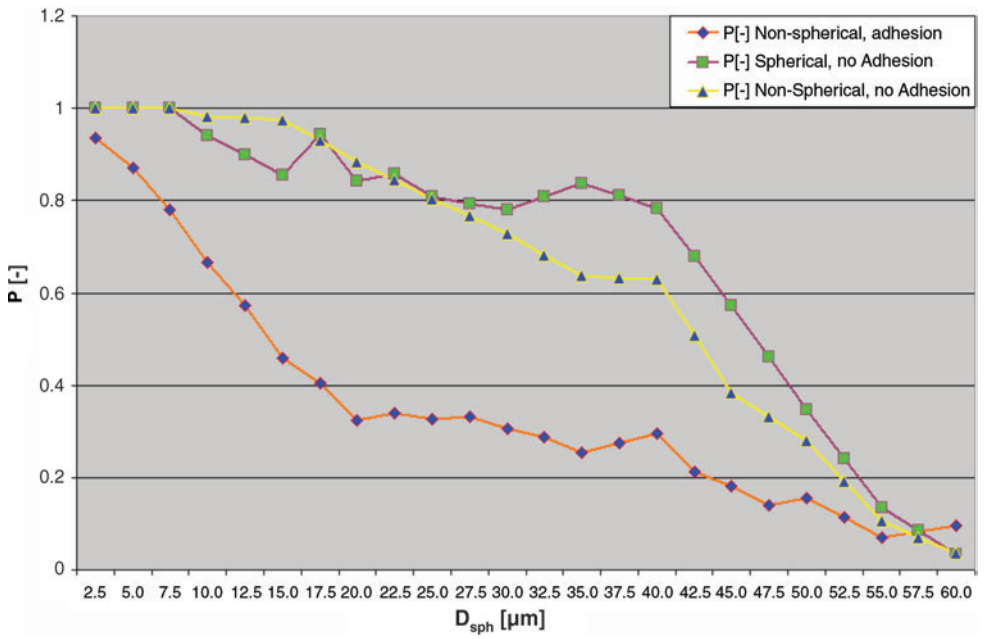

Figure 17 Comparison of particle penetration depth curves for one and the same fibre geometry (see Figure 14). Case a) (purple) is calculated with spherical particles and no adhesion, case b) (yellow) is calculated with non-spherical particles and no adhesion and case c) (orange) is calculated with non-spherical particles and with adhesion. Test case parameters match those, given for Figure 15.

As expected, the adhesional case (orange) shows remarkably lower P-values over the entire, relevant particle size regime, than the non-adhesional cases (yellow and purple). The relationship between particle penetration depth and filter fibre efficiency is demonstrated by comparing spherical and non-spherical, non-adhesional cases in both Figure 16 and 17. For D_{sph}>20µm, non-spherical particles yield smaller penetration values than mass equivalent spheres. This corresponds with the fact, that filter fibre efficiencies for larger ellipsoids are higher.

5 CONCLUSION

A non-spherical dirt particle model for filtration applications has been programmed using the Open Source CFD tool box OpenFOAM®. While a previously published article [3] has presented the most important, underlying concepts behind the new solver. This work has focused on the modelling of particle interaction events, the verification of solver functionality and the presentation of some initial results as well as solver capabilities.

Event force concepts to simulate particle-particle, particle-wall and particle-fibre interaction have been devised. Now a full, four-way coupling (particles-fluid-particles) can be realised. Moreover a controlled, user definable particle-fibre deposition scheme, in accordance with the *force modelling concept* [3] is now in place. Based on the geometrically versatile shape of ellipsoids, dirt particles, that feature 6 degrees of motional freedom, can now be modelled as they make their way through digitally reconstructed, realistic filter fibre geometries. A wide variety of particle shapes, - anything from plates to sticks to simple spheres -, can be approximated by this concept. The particles can interact with the fibre structure, the fluid and among each other. Special, Python [11] based evaluation tools have been created to extract relevant result parameters from the OpenFOAM® text file output. Thus new insight into the progression of important filtration process parameters, such as pressure drop, filtration efficiency and particle penetration depth can now be gained. The entire, computational development effort, as presented in [3], [4] and here, has entailed several important sub steps. They are summarized in Figure 18.

Article [3]: "Basic concepts and fluid-particle force implementation."	Article [4]: "Adaptive time stepping."	This article: "Interaction modelling and validation."
Design of an explicit, force- and torque vector model, which reduces the modelling to the mere formulation of single force effects.	Introduction of an adaptive time stepping scheme for explicit Euler discretization of the PME.	Development of an exact and faster, non-spherical particle–particle collision scheme.
Device of a surface help point scheme to account for large particle effects in terms of fluid particle, particle–fibre, particle–wall and particle–particle interaction.		Implementation of a stable, versatile particle–wall interaction model.
A novel drag force implementation that uses a combination of non-spherical, semi-empirical drag force formulas [7], a panel method to consider free flow swirling effects, a plugging method to include inter particle and particle–fibre hydrodynamics and a simple adaptation of basic concepts known from the immersed boundary method [8].		Implementation of a detailed particle–fibre interaction and deposition model.
Implementation and description of an efficient particle–fluid, two-way coupling method [2].		

Figure 18 Overview of the entire computational development effort in direct relation with this paper.

Due to the object oriented nature of the underlying programming language C++, it is easy to include the fully developed particle module into any laminar, continuum based, Eulerian fluid solver. Additional particle features, like electro-magnetic interaction or diffusion influence on particle motion could be added with comparably little effort. Plans like the integration of a fully versatile chemistry model are harder to realise but not impossible.

Of course validation is important too. Solver functionality as well as qualitative and quantitative result-related aspects have been tested. Two kinds of result-verification were used: comparison with semi-analytical calculations and comparison with experimental results. While a scheme of analytical validation has been devised and extensively discussed

in this work, the ongoing efforts, concerning experimental verification have not yet been published.

In the future, this CFD tool will enable the virtual, purely digital pre-design of filter fibre materials. It will then be possible to upload artificially created fibre structures, conduct the CFD analysis and to consequentially use the results as a good estimate on the expected performance of the newly designed fibre material.

6 REFERENCES

1. M. Mataln, G.Boiger, W. Brandstätter, B. Gschaider, (2008). Simulation of Particle Filtration Processes in Deformable Media, Part 1: Fluid-Structure Interaction, ICE Stroemungsforschung GmbH., Montanuniversitaet Leoben. *Int.Journal of Multiphysics, Vol.2,†No.2, July 2008 , pp. 179–189(11)*;
2. G. Boiger, M. Mataln, W. Brandstätter, B. Gschaider, (2008). Simulation of Particle Filtration Processes in Deformable Media, Part 2: Large Particle Modelling, ICE Stroemungsforschung GmbH., Montanuniversitaet Leoben. *Int.Journal of Multiphysics, Vol.2, No.2, July 2008 , pp. 191–206(16)8;*
3. G. Boiger, M. Mataln, W. Brandstätter, (2009). Simulation of Particle Filtration Processes in Deformable Media, Part 3.1: Basic concepts and particle-fluid force implementation of a non-spherical dirt particle solver, ICE Stroemungsforschung GmbH., Montanuniversitaet Leoben. *Article in review since Jan 2009. Int.Journal of Multiphysics, Vol.3, No.4, March 2010 , pp. 407–232(26);*
4. G. Boiger, M. Mataln, W. Brandstätter, (2009). Adaptive time stepping for explicit Euler implementation of spherical and non-spherical particle speed up. ICE Stroemungsforschung GmbH., Montanuniversitaet Leoben. *Int.Journal of Multiphysics; Vol.3, No.3, August 2009 , pp. 267–291(25);*
5. W.J.Kowalski, W.P.Bahnfleth, T.S.Whittam, (1999). Filtration of Airborne Microorganisms: Modelling and Prediction. Pennsylvania State University, 1999. ASHRAE Transactions 105(2), 4-17. http://www.engr.psu.edu/ae/iec/abe/publications .
6. C.L.Cox, E.W.Jenkins, P.J.Mucha, (2005). Modelling of Debris Deposition in an Extrusion Filter Medium. Clemenson University, Clemenson, SC. Proceedings of the 21st Annual Meeting of the Polymer Processing Society, Leipzig, Germany, June 19–23, 2005.
7. A. Hölzer,& M. Sommerfeld, (2007). New, simple correlation formula for the drag coefficient of Non – Spherical Particles. Martin-Luther-Universität, Halle-Wittenberg, Germany. *Powder Technology, Vol.184(3) (2007), 361–365.*
8. C.S. Peskin, (2002). The immersed boundary method, Cambridge University Press, Acta Numerica 2002, pp.1–39, DOI: 10.1017/S0962492902000077.
9. K.B.Shah, M.Megahed, (2005). Discrete and Chimera Particle Simulation: Novel LaGrangian Extensions and Applications, ESI-Group, Germany. Industrial two-phase flow CFD, 2005. VKI LS 2005–04; Vol.1.
10. M. Mataln, W. Brandstätter, (2004). A Unified Approach to Model Fluid-Structure Interactions, Montanuniversitaet Leoben, Austria. *Society of Petroleum Engineering, seminar notes, 2004.*
11. M.Lutz, (2005). Python. Kurz&Gut, Köln: O'Reilly Verlag 2005. ISBN: 3-89721-511-X.
12. W.C.Hinds, (1999). Aerosol technology: properties, behavior, and measurement of airborne particles, New York: Wiley 1999. ISBN: 0471194107 9780471194101.
13. W.B.Jones, W.J.Thron, (1980). Continued Fractions: Analytic Theory and Applications, Cambridge University Press 2009. ISBN-10: 0521101522.
14. M.Sommerfeld, (2007). Fundamentals of Particles, Droplets and Bubbles. Martin Luther Universität, Halle-Wittenberg, Germany. SIAMUF-Seminar and workshop, Chalmers University of Technology, October 2007.